Probing the Chemical State of Tin Oxide NP Catalysts during CO_2 Electroreduction: A Complementary *Operando* Approach

Abhijit Dutta[a], Akiyoshi Kuzume[b], Veerabhadrarao Kaliginedi[a], Motiar Rahaman[a], Ilya Sinev[c], Mahdi Ahmadi[d], Beatriz Roldán Cuenya[c], Soma Vesztergom[e,*], Peter Broekmann[a,*]

[a] *University of Bern, Department of Chemistry and Biochemistry*
Freiestrasse 3, 3012 Bern, Switzerland
[b] *Tokyo Institute of Technology, Institute of Innovative Research*
Nagatsuta-cho 4259, 2268503 Yokohama, Japan
[c] *Fritz Haber Institute of the Max Planck Society*
Faradayweg 4–6, 14195 Berlin, Germany
[d] *Cornell University, Department of Chemistry & Chemical Biology*
East Ave 245, 14850 Ithaca NY, USA
[e] *Eötvös Loránd University, Department of Physical Chemistry*
Pázmány Péter sétány 1/A, 1117 Budapest, Hungary

Abstract

In this paper we combine two *operando* methods, Raman spectroscopy and X-ray absorption spectroscopy (XAS), in order to probe graphene-oxide supported tin^{IV} oxide nanoparticles (SnO_2NPs@rGO) as they are being used to catalyse CO_2 electroreduction. To achieve high reaction rates it is necessary to apply sufficiently cathodic electrode potentials. Under such conditions, however, not only CO_2 is reduced electrochemically, but also the catalyst particles may be transformed from the initial Sn^{IV} state to Sn^{II} or, in an extreme case, to metallic Sn. While Sn^{II} species still favour CO_2 electroreduction, yielding formate as a primary product, on metallic Sn CO_2 reduction is disfavoured with respect to the competing hydrogen evolution reaction (HER). We show that *operando* XAS, a robust technique yielding information averaged over a large surface area and a relatively large thickness of the catalyst layer, is a very expedient method able to detect the reduction of SnO_2NPs@rGO to metallic Sn. XAS can thus be used to establish an optimum potential for the electroreduction in practical electrolysing cells. It takes, however, a complementary method offered by *operando* Raman spectroscopy, having greater sensitivity at the catalyst/electrolyte solution interface, to probe reduction intermediates such as the Sn^{II} state, which remain undetectable for *ex situ* methods. As it is shown in the paper, Raman spectroscopy may also find further use when investigating the recovery of catalyst particles following exposure to extreme reducing conditions.

Keywords: power to value, Raman spectroscopy, X-ray absorption spectroscopy, carbon dioxide electroreduction, catalyst recovery

1. Introduction

Today the scientific community agrees to that the recent increase of atmospheric CO_2 levels is primarily related to human activities like the use of fossil fuels and the mass destruction of forests. The natural buffers of our planet — like oceanic or photosynthetic uptake — seem unable to cope with the large amount of human-generated CO_2; thus, preserving our environment from the threats related to anthropogenic CO_2 emissions is one of the greatest challenges facing our society today [1].

The chemical transformation of CO_2 into organic molecules [2] may become a possible way to decrease atmospheric CO_2 concentrations. By the (electro-)chemical reduction of CO_2, we can create other molecules like carbon monoxide, formic acid or methanol, which we may then use as chemical feed-stock and turn into other value-added products. It is at this time a matter of debate whether this process is profitable or not [3–5]; it can be argued, nonetheless, that the electrochemical reduction of such an inert molecule as CO_2 has a very considerable fundamental and practical appeal [6]. This is the reason for which the electroreduction of CO_2, first described more than 150 years ago [7], has gained a lot of attention lately [8–18].

*Corresponding authors.
Email addresses: abhijit.dutta@dcb.unibe.ch (Abhijit Dutta), kuzume.a.aa@m.titech.ac.jp (Akiyoshi Kuzume), bhadra.chemistry@gmail.com (Veerabhadrarao Kaliginedi), motiar.rahaman@dcb.unibe.ch (Motiar Rahaman), ilya.sinev@ruhr-uni-bochum.de (Ilya Sinev), ma2259@cornell.edu (Mahdi Ahmadi), roldan@fhi-berlin.mpg.de (Beatriz Roldán Cuenya), vesztergom@chem.elte.hu (Soma Vesztergom), peter.broekmann@dcb.unibe.ch (Peter Broekmann)

Like in any fields of electrocatalysis research, the primary concern when studying the electroreduction of CO_2 is to identify catalysts that can selectively yield a desired product with a suitable rate and energy efficiency. In the quest for finding new catalyst materials, however, the demand for robustness is often overlooked, although the stability of catalytic systems should remain a key question of research. This becomes immediately apparent when certain "metal oxide type" catalysts [19] are used for the catalysis of an essentially cathodic reaction, such as the electroreduction of CO_2.

To achieve any considerable turnover in CO_2 electroreduction, significantly large (negative) electrode potentials have to be applied. Such harsh cathodic conditions, however, will not only boost the electrolysis of CO_2 but may also lead to a potential-induced reduction of the oxide catalyst particles, accompanied by often irreversible size and morphology changes and a resulting catalyst degradation. Such changes can have an unwanted effect on both the overall rate of the catalysed process, as well as on the selectivity towards the formation of a desired product.

An illustrative example of a degrading metal oxide catalyst is tin oxide. It has long been known [20] that on Sn-related electrodes the electroreduction of CO_2 selectively yields formate or formic acid. Studies of CO_2 electroreduction recently carried out on metallic tin [21–33] and on various forms of Sn oxides [34–50] reported, however, very different Faradaic efficiencies of formate production, with *FE* values ranging between 10 and 90%.

The scatteredness of the reported *FE* values hints that the electrocatalytic activity of Sn and Sn oxide catalysts strongly depends on many experimental factors such as the oxidation state, morphology, and particle size of the catalyst, the composition of the electrolyte and the electrode potential applied for the electrolysis [50].

It seems likely that among the many experimental factors affecting the product yield of CO_2 electroreduction the oxidation state of the interfacial Sn atoms plays a crucial role. For example, Chen and Kanan [35] studied the activity of Sn electrodes that had been subjected to different pre-electrolysis treatments in order to reduce (or in some cases, to increase) the thickness of the surface oxide layers. They found that once the native surface oxide layer of a tin electrode was removed (*i.e.*, the electrolysis was practically carried out on bare metallic Sn), the *FE* for the production of formate dropped down to practically zero. On the other hand, by using Sn catalysts with an artificially increased oxide layer thickness, Chen and Kanan measured at least four times higher *FE*s for formate production (compared to the formate yield of the metal covered by its native oxide layer) [35].

The results of the Kanan group [35] were further supported by a few other studies on tin oxide films or SnO_x nanoparticles of different kinds [36–46, 50]. A clear conclusion of all these studies is that while using SnO_x — either in a film or in a nanoparticulate form — for the catalysis of CO_2 reduction, the oxidation state of the catalyst cannot always be maintained at the highly cathodic operating conditions, and the reduction of the catalyst may result in a loss of catalytic activity or a reduced selectivity toward the production of formate.

We should note, however, that the above conclusion is usually supported in the literature based on the results of *ex situ* analyses. For instance, Chen and Kanan [35] used *ex situ* X-ray photoelectron spectroscopy (XPS) in order to show the structural effects of etching (surface oxide removal) of Sn electrodes. Shiratsuchi *et al.* [36] used XPS in order to demonstrate structural changes of their catalyst after various times of electrolyses. Meyer *et al.* [37] applied transmission electron microscopy (TEM) and X-ray diffraction spectroscopy (XRD) — prior to the electrolysis — to determine particle sizes, which they then correlated to the measured *FE*s. Lee *et al.* [38] applied XRD and also XPS (both *ex situ*) to study the structural changes that electrolyses treatments for different times introduced to their catalyst.

As opposed to the former approaches, we favour the use of *operando* spectroscopic techniques [50–61], since we believe that these methods can give a better insight into the structural and chemical changes that SnO_2 catalysts undergo as they are used for catalysing the CO_2 electroreduction process. In this paper we study graphene-oxide supported tin^{IV} oxide nanoparticles (SnO_2NPs@rGO) as a model catalyst for CO_2 electroreduction. It is known [50] that under the operating conditions of the electrolysis — that is, at negative electrode potentials — the Sn^{IV} in SnO_2NPs@rGO can undergo reduction to Sn^{II} or, in an extreme case, to metallic Sn (Figure 1). While Sn^{II} species favour CO_2 electroreduction, yielding formate as a primary product, on metallic Sn, CO_2 reduction is disfavoured with respect to the competing hydrogen evolution reaction (HER) [50].

In this work, we combine two *operando* methods, Raman spectroscopy and X-ray absorption spectroscopy (XAS), in order to probe oxidation state, size, and morphology changes of the SnO_2NPs@rGO catalyst.

In order to carry out reliable *operando* XAS measurements, significant absorbances must be achieved [62]. In a typical experimental configuration, passing the X-ray beam through the electrolyte layer is avoided; instead, the beam impinges on the back of the sample and has to pass a relatively thick catalyst layer. As a result, it yields information convoluted over a relatively large volume. Nevertheless, XAS can detect, for example, the reduction of the Sn^{IV} catalyst species to metallic Sn at large negative electrode potentials. This makes *operando* XAS an expedient method of establishing optimum electrolysis potentials in practical CO_2 electrolysing cells [63]. By XAS, information on the chemical state of the carbon supported oxidic catalyst can be obtained even under massive gas evolution conditions.

A mechanistic understanding of catalyst degradation requires, however, a method that is more sensitive to the catalyst/electrolyte solution interface, such as *operando*

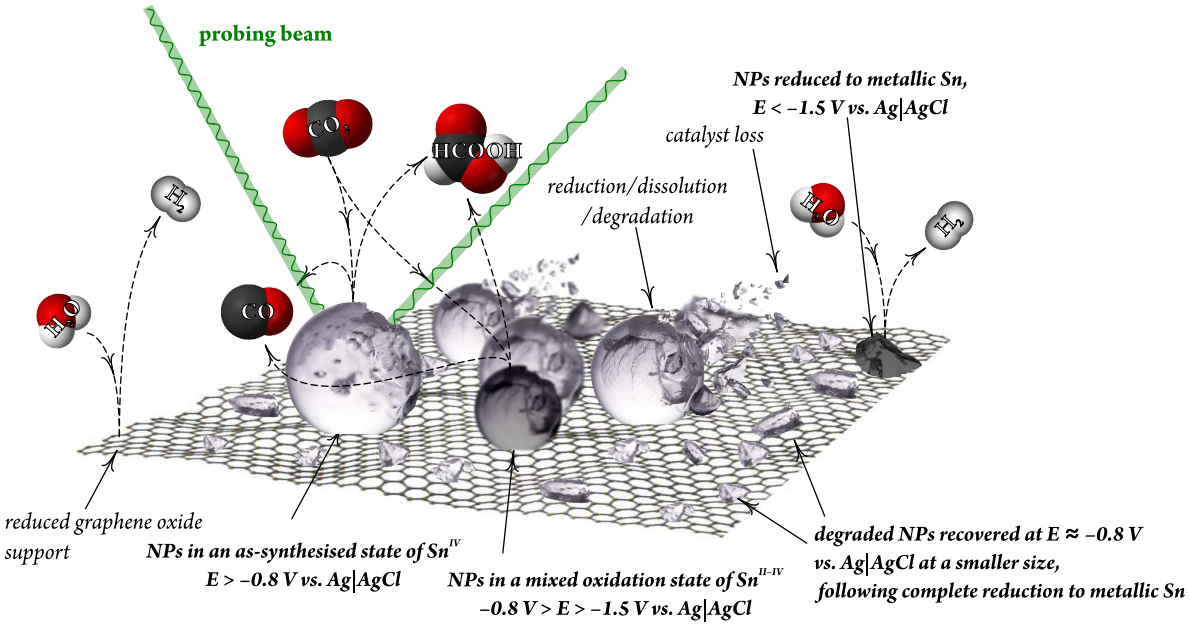

Figure 1: SnO_2NPs@rGO catalyst used for the electroreduction of CO_2 molecules. At more and more cathodic potentials, the catalyst gets chemically reduced and the size of the NPs shrinks. At moderately cathodic potentials, when the SnO_x catalyst is in a mixed oxidation state ($1 < x < 2$), the catalyst exhibits a maximal Faradaic efficiency for the production of formate. At extremely cathodic potentials, the catalyst NPs are reduced to metallic Sn and the selectivity towards formate production drops.

Raman spectroscopy. As opposed to XAS, the application of *operando* Raman spectroscopy requires the use of thin SnO_2NPs@rGO layers where no intense gas formation prevents the focusing of the Raman beam. When properly applied, Raman spectroscopy is capable to detect certain reduction intermediates — such as oxide particles in the Sn^{II} state — that otherwise remain undetectable in particular for *ex situ* methods. As it is shown in the paper, Raman spectroscopy may also find further use when investigating size and morphology changes of the catalyst NPs. Furthermore, *operando* Raman spectroscopy is also expedient when our aim is to study the recovery of catalyst particles following exposure to extreme reducing conditions.

In what follows, we compare *operando* XAS and *operando* Raman methods and their abilities to detect the potential-induced degradation of SnO_2NPs@rGO catalysts, as they are being used for the electrolysis of CO_2.

2. Materials and Methods

2.1. Synthesis

The poly(vinylpyrrolidone) (PVP) modified SnO_2NPs@rGO catalyst was prepared exactly as it was described elsewhere [50]. For the measurements presented in this paper, the catalyst was used in the form of an ink that was created by mixing 5 mg of the PVP-modified rGO-supported SnO_2 NPs with 0.1 cm^3 of a 5 wt% Nafion™ ionomer solution (analytical grade, Sigma Aldrich), 0.7 cm^3 Milli-Q water and 0.2 cm^3 2-propanol (Sigma Aldrich). Catalyst loadings reported in the paper (in units of mg cm^{-2}) refer to the mass of SnO_2NPs@rGO (and not of the ink), normalized with the geometric surface area of the working electrode support.

2.2. Instrumentation

X-ray diffraction (XRD) analysis was done on a Seifert 2000 diffractometer with Cu–Kα radiation. Scans were recorded between 20° to 100°; the particle size was determined on the basis of Scherrer's equation, and Bragg's formula was used for the determination of the lattice parameter [50].

X-ray photoelectron spectroscopy (XPS) studies were carried out using Al–Kα radiation sources at 150 W with an Omicron Multiprobe spectrometer and an EA125 hemispherical analyser (Omicron Nano Technology) [50].

Transmission electron microscopy (TEM) analysis was carried out by suspending the catalyst on a Cu grid with 300 meshes. The applied accelerating voltage was 200 kV on a FEI Tecnai G2 T20 S-Twin instrument [50].

Raman spectroscopy was performed using a LabRAM HR800 confocal microscope (Horiba Jobin Yvon) [50]. A long working distance objective lens (50 times magnification, 8 mm focal length) was used with a numerical aperture of 0.1 in order to focus a diode-pumped solid-state laser beam (excitation wavelength 532 nm, power 3 mW) on the sample. The Raman signal was collected in a back-scattering geometry, using a custom-made spectro-electrochemical cell. For *operando* Raman experiments, the catalyst was drop-cast on a glassy carbon

support, used as a working electrode. The electrode potential was measured vs. an Ag | AgCl | 3.4 mol/dm^3 KCl reference electrode (eDAQ ET072), and a Pt wire was applied as an auxiliary electrode. An Autolab 302N (EcoChemie) potentiostat was applied. Electrolyte solutions for the *operando* Raman experiments were prepared by bubbling CO_2 through a 0.5 mol dm^{-3} solution of NaOH until a desired pH value was reached [50].

Ion and gas chromatography was used to determine the product distribution of CO_2 electroreduction. A custom-built, air-tight, two-compartment (H-type) cell of known compartment volumes was applied [64]. A three-electrode arrangement was used, in which the SnO_2NPs@rGO catalyst ink, drop-cast on a glassy carbon support, served as a working electrode. The cell contained a leakless Ag | AgCl | 3.4 mol/dm^3 KCl reference electrode (eDAQ ET072) and a bright Pt foil (15 mm × 5 mm) counter electrode as well, the latter placed in a different compartment separated from the working electrode compartment by a polymer membrane (Nafion 117, Sigma-Aldrich). For the analysis of product distribution, different catalyst loadings were applied, as noted in the text. Prior to electrolysis, the working and counter electrode compartments were both filled with 30 cm^3 of 0.5 mol dm^{-3} NaOH solution. The solutions were purged with CO_2 gas (99.999%, Carbagas), until the pH value required by the experiment was reached. To enhance the mass transport of CO_2 towards the cathode, the catholyte was continuously stirred by magnetic agitation. Electrolyses, usually lasting for 1 hour, were carried out at constant potentials. The current of the electrolysis was constantly monitored and integrated over time in order to determine the charge yield. The head-space of the catholyte compartment was continuously purged with CO_2 in order to transport all the volatile reaction products from the head-space into the sampling loops of the online gas chromatograph (SRI Instruments). The partial current density for a given gaseous product k was determined by using Equation (1):

$$I_k = x_k \, n_k \, F \, v_{\mathrm{m}}, \tag{1}$$

where x_k is the mole fraction of product k in the analysed sample (determined based on calibration), n_k is the number of electrons involved in the reduction reaction that forms product k, v_{m} is the molar flow rate of CO_2, and F is Faraday's constant. The partial current was integrated over the time of the electrolyses to yield a partial charge that was then related to the total charge consumption of the experiment, thus providing the *FE* of the given product. By means of GC, only two gaseous products — H_2 and CO — were detectable.

In order to calculate the Faradaic efficiency of $HCOO^-$ production, we applied an ion chromatograph (Metrohm) consisting of an L–7100 pump, a conductivity detector, a separation and an exclusion column (Metrosep A Supp 7–250), to measure formate concentrations following electrolysis: the amount of produced formate was related to the charge consumed by the electrolysis [50]. By the means of chromatographic analysis, $HCOO^-$, CO and H_2 were the only detectable products, accounting — within range of experimental error — for an altogether 100% Faradaic efficiency.

X-ray absorption spectra (XAS) were acquired at the Samba beam-line of the Soleil synchrotron facility in Saint-Aubin, France. The spectra were collected at the Sn-K edge (29.2 keV) in fluorescence mode, using a 35-element Ge detector (Canberra). A home-built *operando* electrochemical cell was used with a 50 × 50 mm Pt mesh counter electrode and a leakage-free Ag/AgCl reference electrode (Innovative Instruments, Inc.). The SnO_2NPs@rGO catalyst sample was deposited on a carbon paper disc (Sigracet, SGL Group) by filtration from a slurry of the sample in ethanol. The paper disc served as a working electrode with the sample-coated side exposed to the electrolyte and the uncoated side remaining dry. The Athena program [65] was used for background removal and isolation of the extended X-ray absorption fine structure (EXAFS) spectra. EXAFS fitting was performed using the Artemis software with theoretical backscatering amplitudes and phase-shifts calculated using the *ab-initio* FEFF6 code. Nearest-neighbour coordination numbers (CN), interatomic distances (R) and disorder parameters (Debye–Waller factors, DWF) were extracted for the fit of the first coordination shell of Sn.

3. Results

3.1. Structural characterization of SnO_2NPs@rGO catalyst

The structure of the SnO_2NPs@rGO catalyst, synthesised from stannous octoate, was studied before [50]. Briefly, the NPs were characterized by an average particle size of (4.4 ± 0.9) nm as shown by transmission electron micrographs (TEM, Figure 2(a)). The NPs were uniformly dispersed on the rGO surface and no aggregation was seen. High-resolution TEM and the corresponding FFT (Figure 2(b)) enabled us to determine an interplanar d-spacing of ∼ 0.334 nm, characteristic for SnO_2 (110) [50].

In X-ray photoelectron spectroscopy (XPS) surveys, signals of Sn, O, and C can be observed [50]. The high-resolution XPS spectrum (Figure 2(c)) shows the binding energies of Sn $3d_{5/2}$ and $3d_{3/2}$ at 486.6 and 495.0 eV, respectively, suggesting a dominant Sn^{IV} oxidation state [50, 66].

In the Raman spectrum of as-synthesised SnO_2NPs@rGO (Figure 2(d)), the peaks at 1355 and 1593 cm^{-1} correspond to the D and G bands of reduced graphene oxide, respectively. Figure 2(d) also displays three other peaks (shown at higher resolution in Figure 2(e)) at 482, 623, and 762 cm^{-1} that can be identified as the E_{g}, $A_{1\mathrm{g}}$, and $B_{2\mathrm{g}}$ modes of SnO_2 crystallites, respectively [50, 67].

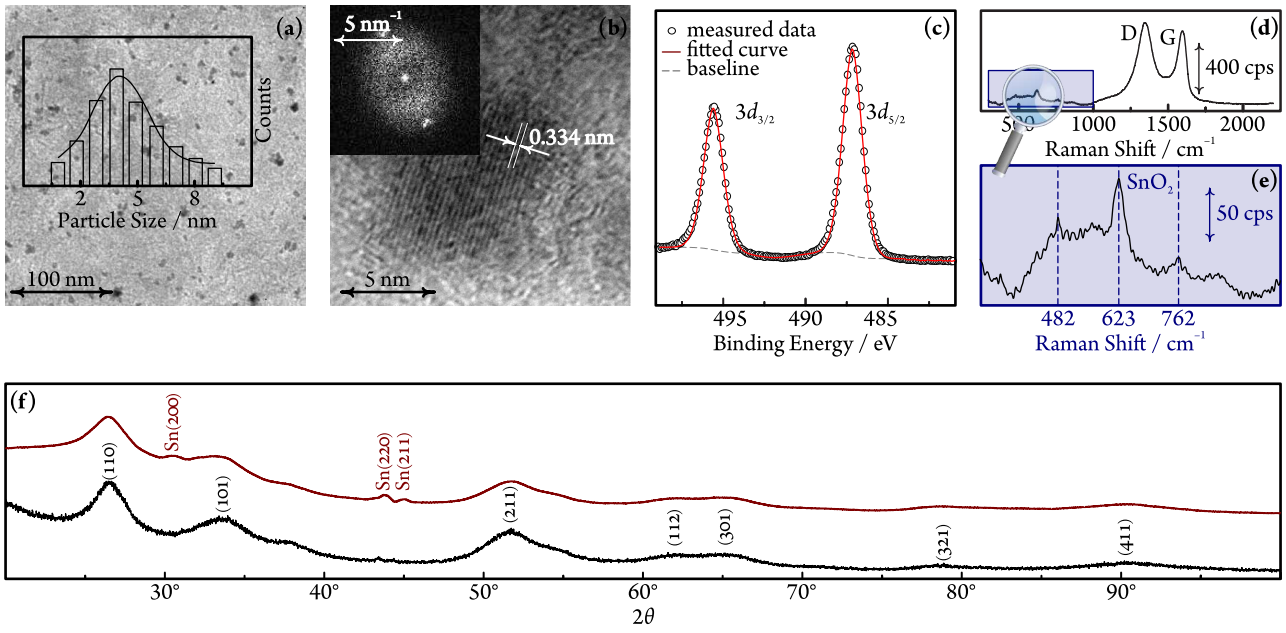

Figure 2: Structure of the SnO_2NPs@rGO catalyst [50]. **(a)** The transmission electron micrograph shows SnO_2 NPs with an average diameter of (4.4 ± 0.9) nm, distributed evenly and without aggregation on rGO. **(b)** The high-resolution TEM image and the corresponding FFT reveal an interplanar d-spacing characteristic for the (110) crystal face of SnO_2. **(c)** The high-resolution XPS spectrum of the Sn $3d$ region suggest that the oxidation state Sn^{IV} prevails in the synthesised catalyst. **(d,e)** Raman spectrum of the as-synthesised catalyst: peaks characteristic for SnO_2 are shown in (e). **(f)** The X-ray diffractograms of SnO_2NPs@rGO show peaks that can be assigned different crystal faces of SnO_2, based on JCPDS–41–1445. The XRD diffraction patterns measured on the same catalyst, following electrolysis at $E = -1.55$ V *vs.* Ag|AgCl in a pH = 8.5 bicarbonate solution (red curve) show additional peaks that can be assigned to crystal faces of metallic Sn (based on JCPDS–04–0673).

The X-ray diffraction (XRD) pattern of SnO_2 NPs (Figure 2(f)) shows peaks characteristic for cassiterite, a SnO_2 phase of tetragonal rutile structure [50].

3.2. Operando XAS investigation of potential-induced oxidation state changes of SnO_2NPs@rGO

The Sn atoms of as-synthesised SnO_2NPs@rGO are practically completely oxidised to the state of +4, as shown by the *ex situ* survey of the catalyst particles (Figure 2). However, when the catalyst particles are being used for the electrolysis of CO_2, and a negative electrode potential is applied to them, the oxidation state of the SnO_2 particles may not be maintained at the original +4 oxidation state, and the catalyst particles can undergo partial or complete reduction.

To investigate oxidation state changes of SnO_2NPs@rGO during CO_2 electroredution, XAS measurements were conducted on the as-synthesised sample and under reaction conditions, by applying −1.15, −1.55 and −1.70 V potentials *vs.* Ag|AgCl. X-ray absorption near-edge structure (XANES) spectra are shown in Figure 3(a). Since the intensity of the XANES peak is mainly determined by the unoccupied density of states (DOS) and higher oxidation states lead to higher unoccupied DOS, one can evaluate the oxidation state of the catalyst through the intensity of the first XANES peak above the edge, the so-called "white line", as well as by the shift in the absorption edge energy.

The position of the Sn K absorption edge, determined as the first maximum of the absorption coefficient, was reported to be 29200, 29202 and 29205 eV for metallic Sn, SnO and SnO_2, respectively [68]. The absorption edge position thus has a seemingly linear dependence on the valence state of Sn in the probed material. The high intensity of the white line, as well as the edge position at 29205 eV in the as-synthesised sample indicates dominating Sn^{IV} species. Since the white line intensity and the edge position did not change when a potential of −1.15 V *vs.* Ag|AgCl was applied, it is apparent that such potential is not sufficient to reduce the catalyst.

By setting a more cathodic potential, −1.55 V *vs.* Ag|AgCl, the white line intensity was found to decrease, and the decrease continued upon setting an even more negative potential, −1.70 V *vs.* Ag|AgCl. The observed changes in the white line intensity were accompanied by an energy shift of the edge position from 29205 eV (characteristic for the as-synthesised state and for the spectrum recorded at −1.15 V *vs.* Ag|AgCl) to 29203.6 and 29202.7 eV at −1.55 and −1.70 V, respectively. The decrease of the edge position indicates a progressive reduction of the Sn species at negative electrode potentials.

In fact, the *operando* XANES spectra can be interpreted as a sum of absorbances related to metallic Sn and to SnO_2. The XANES spectra of these two reference states are also plotted in Figure 3(a). In Figure 3(b) it is shown

(E *vs.* Ag|AgCl) /V	Composition / %		Sn–Sn Scatters			Sn–O Scatters		
	SnO_2	Sn	*CN*	*R*/Å	*DWF*	*CN*	*R*/Å	*DWF*
as-synthesised	100	0	—	—	—	3.0 ± 0.1	2.05 ± 0.01	0.0030 ± 0.0005
−1.15	98.4 ± 0.7	1.6 ± 0.7	—	—	—	3.1 ± 0.1	2.05 ± 0.01	0.0030 ± 0.0004
−1.55	66.6 ± 0.6	33.4 ± 0.6	1.6 ± 0.3	3.02 ± 0.01	0.010 ± 0.001	2.1 ± 0.1	2.04 ± 0.01	0.0050 ± 0.0008
−1.70	40.5 ± 0.5	59.5 ± 0.5	2.7 ± 0.4	3.02 ± 0.01	0.010 ± 0.002	1.3 ± 0.2	2.00 ± 0.01	0.0070 ± 0.0010

Table 1: Summary of the XAS analysis of SnO_2NPs@rGO. Oxidation state (composition) analysis was carried out based on the Sn K-edge XANES spectra of Figure 3(b). Fitting parameters, such as the nearest-neighbour coordination number (*CN*), the inter-atomic distance (*R*) and the Debye–Waller factor (*DWF*) were extracted from the single scattering analysis of the EXAFS spectra of Figure 4; signals from Sn–Sn and Sn–O scatters were considered.

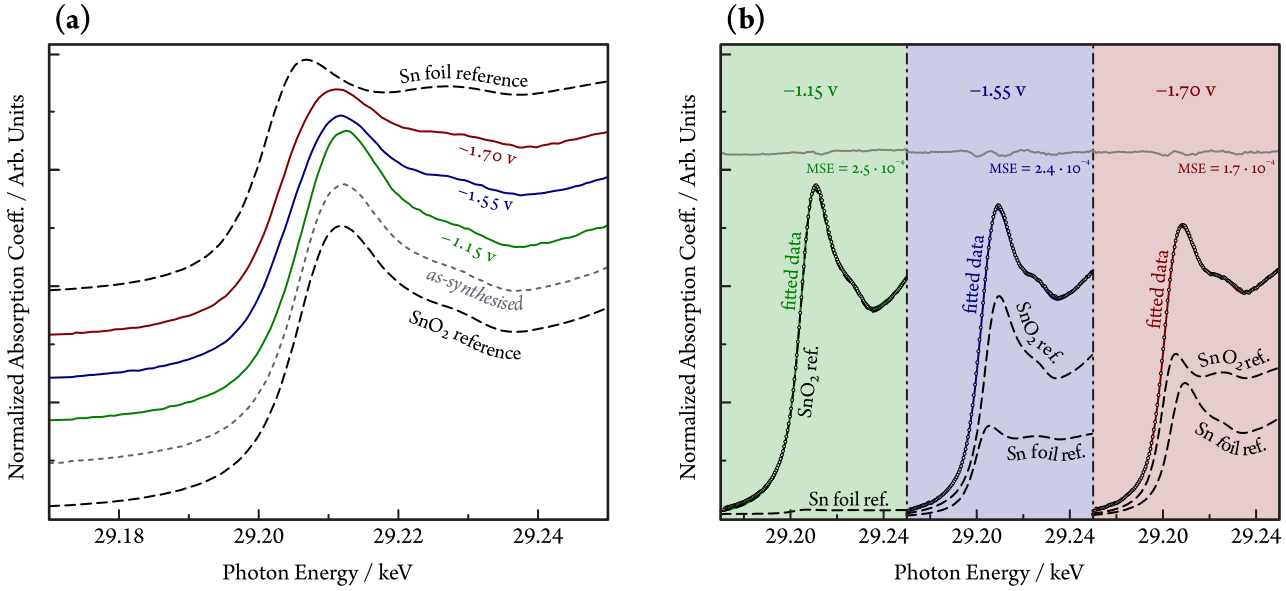

Figure 3: **(a)** Sn K-edge XANES of the SnO_2NPs@rGO catalyst, acquired *operando*, at different electrode potential values (marked in the figure *vs.* Ag|AgCl). Spectra of pure SnO_2, of pure metallic Sn and of the as-synthesised SnO_2NPs@rGO, measured at the same beam-line under identical conditions, are also plotted as a reference. **(b)** At each applied potential, the absorbance of SnO_2NPs@rGO is a linear combination of absorbances related to Sn and SnO_2. Weighted spectrum components corresponding to Sn and SnO_2 are plotted as dashed curves: the sum of these fit the measured data (empty circles) reasonably well, as shown by the full curves. The mean squared error (MSE) of the fit is shown by the grey curves, shifted along the vertical scale for better visibility. Measurements were carried out at *p*H=8.5, applied catalyst loading: 5 mg cm^{-2}.

that by a linear combination of the two reference states, the *operando* XANES spectra of SnO_2NPs@rGO can very well be reproduced, with small mean squared error (MSE) values. Based on the weights of the reference spectra, the oxidation state of SnO_2NPs@rGO can be estimated at the applied potentials, as shown in Table 1.

The above observations are in agreement with the results of Fourier-transformed extended X-ray absorption fine structure spectroscopy (EXAFS), as demonstrated by Figure 4. EXAFS spectra measured on the as-synthesised catalyst and at mild cathodic polarization ($E = -1.15$ V *vs.* Ag|AgCl) show an intense peak at 155 pm (phase uncorrected), typical for SnO_2 [69], while the peaks at higher distances are less intense, reflecting small particle size or a highly disordered structure.

At −1.55 V *vs.* Ag|AgCl, a peak appears at 280 pm, corresponding to Sn–Sn scattering in the metallic tin structure [69]. It becomes more intense at −1.70 V, while the Sn–O feature decreases. Fitting the EXAFS spectra with Sn–O and Sn–Sn back-scattering confirms the conclusions drawn above, which are summarized in Table 1. The Sn–O coordination number is 3.0 for the sample in the as-synthesised state and at -1.15 *V*; it decreases to 2.1 and 1.3 at −1.55 and −1.7 V *vs.* Ag|AgCl, respectively. The coordination number of the metallic Sn–Sn state at −1.55 V, where it is first observed, is 1.6 and increases to 2.7 at −1.70 V.

Notably, the two most dominant peaks in the EXAFS spectra can be assigned to either metallic Sn or Sn^{IV} species, as also shown by the fair fit of Figure 4. Apparently, Sn^{II} signals are not abundant in the EXAFS spectra, although the small peak-like feature at about 205 pm may be assigned to this intermediate oxidation state [70].

3.3. Operando Raman insight into potential-induced catalyst degradation and successive recovery

For the successful application of *operando* XAS, *i.e.*, to achieve measurable absorbances, a relatively thick catalyst layer was applied. As indicated in the caption of Figs. 3 and 4, by spreading the prepared catalyst ink

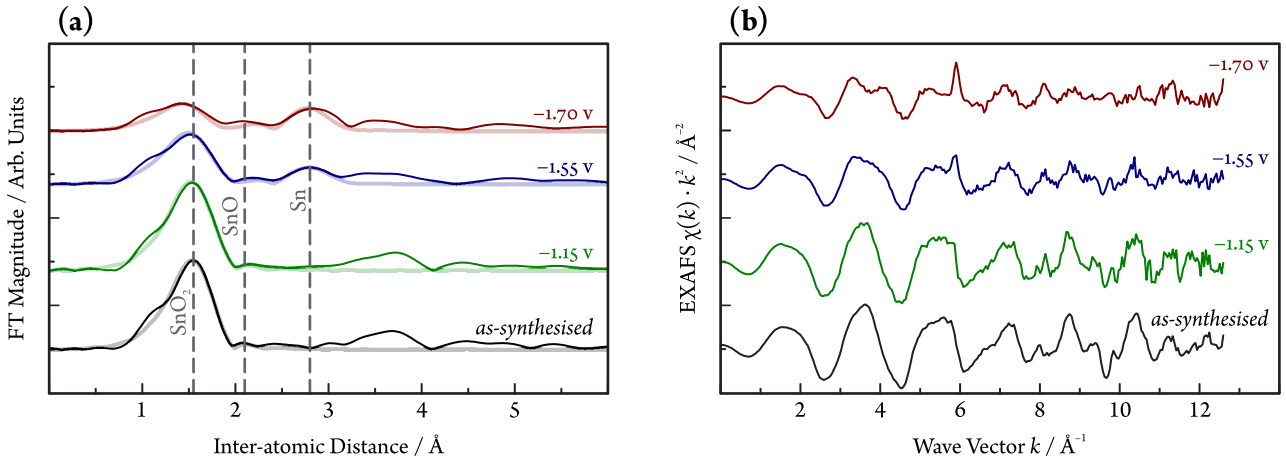

Figure 4: **(a)** k^2-weighted Sn K-edge Fourier transform EXAFS spectra of SnO_2NPs@rGO, acquired *operando*. The fits to the EXAFS spectra are shown as faded thick curves and correspond to a combination of Sn–Sn and Sn–O scattering paths. **(b)** EXAFS measurement results shown in k-space. Measurements were carried out at pH=8.5, applied catalyst loading: 5 mg cm^{-2}.

(see the Methods section for more detail) over a carbon paper support, we achieved a loading of 5 mg cm^{-2} (for SnO_2NPs@rGO); that is, a relatively thick catalyst layer. As a result, the gathered XANES and EXAFS spectra are not only characteristic for the electrolyte solution/catalyst interface, but they also carry information from deeper catalyst layers that may not be in direct contact with the solution.

As opposed to XAS, which we used in a fluorescence mode, *operando* Raman is a scattering spectroscopy. This makes Raman more sensitive to the catalyst/electrolyte solution interface, yielding a deeper insight into the potential-induced oxidation state, size and morphology changes of SnO_2NPs@rGO as they are applied for the electrolysis of CO_2.

In Figure 5(a) we show the results of *operando* Raman experiments. Here the electrode potential was gradually stepped from less cathodic (−0.25 V) to more cathodic values (−1.55 V *vs.* Ag|AgCl) in a pH = 8.5 bicarbonate solution, while at each applied potential, Raman spectra of the SnO_2NPs@rGO catalyst were acquired. Closer inspection of Figure 5(a) reveals a peak at $\sim$ 623 cm^{-1} that is present at all potentials above −1.25 V but quickly decays at $E \leq -1.25$ V. A second notable feature of the spectra is another peak at $\sim$ 218 cm^{-1} that is not present in the as-synthesised catalyst. This second peak first appears at $E \leq -0.6$ V and then disappears again at $E \leq -1.5$ V.

Based on literature, the two peaks can be assigned to tin oxide species of different oxidation states. The peak at 623 cm^{-1} corresponds to the A_{1g} vibration mode of SnO_2 crystallites [72], and the relatively narrow peak width is in accordance with the 4–5 nm average diameter of the NPs [72]. The other peak at 218 cm^{-1} can be assigned to the A_{1g} vibration mode of SnO species [73, 74]. The relative intensities of the mentioned peaks are plotted as a function of the electrode potential in Figure 5(b).

Compared to *operando* XAS, the potential-evolution of the various Raman peaks gives additional information as to the chemical and morphological changes of the catalyst occurring in the course of CO_2 electroreduction. As it is shown in Figure 5(a) and (b), the intensity of the SnO_2 related peaks first decreases mildly, together with the appearance of a SnO related feature. Later, at very negative potentials the spectroscopic fingerprints of both oxide forms disappear as the catalyst is entirely reduced to metallic Sn. Here we note that the presence of metallic Sn can be experimentally proven also by *ex situ* methods like XRD, following electrolysis (see the diffractogram drawn with a red curve in Figure 2(f)).

Following potential excursions to very negative potentials (resulting in the formation of metallic Sn), the SnO_2 NPs may only be recovered partially, and in a size much smaller compared to the as-synthesised NPs. Figure 5(c) shows Raman spectra measured *operando* during a "recovery" attempt. The electrode potential was here scanned backwards (from negative toward positive values), starting the scan at a fully reduced state. There is only one notable feature of these spectra: the development of a broad peak centred at approximately 580 cm^{-1}. Literature data [72] allows the interpretation of this peak as an overlap of disorder related surface modes of SnO_2 particles with significantly smaller size (2–3 nm) compared to that of as-synthesised NPs (4–5 nm). It should also be noted that as opposed to Figure 5(a), the spectra of Figure 5(c) do not show any sign of SnO-related features.

Practically the same happens if instead of gradually stepping back the potential to more positive values, we — following a full reduction lasting several minutes at −1.55 V — set the potential directly to −0.25 V and wait for the recovery of SnO_2 NPs (see Figure 6 for the time dependence of the acquired Raman spectra). The fact that following extreme negative potential excursions we can only recover NPs of smaller size can probably be explained by a degradation of the oxide as it is reduced

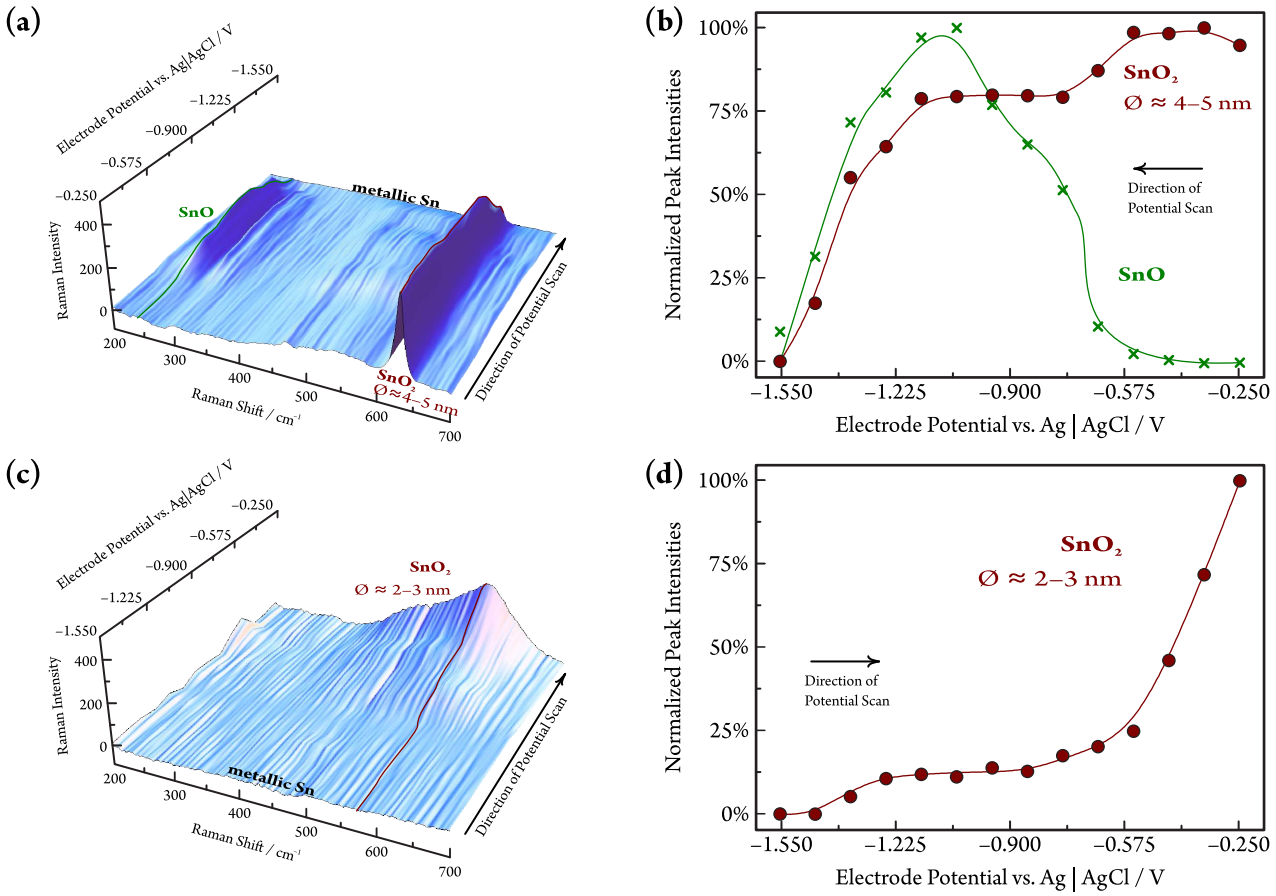

Figure 5: **(a)** Three-dimensional surface plot of Raman intensities created by a continuous acquisition of Raman spectra as the electrode potential was slowly stepped from less (−0.25 V) to more negative values (−1.55 V *vs.* Ag|AgCl). **(b)** The intensities of SnO_2 and SnO related peaks as a function of the electrode potential; the lines here correspond to those shown on the surface plot in (a). **(c)** Potential-dependent Raman spectra recorded in the course of stepping the potential back from –1.55 V to –0.25 V *vs.* Ag|AgCl. **(d)** The intensity of the SnO_2 related wave as a function of the electrode potential; the line here corresponds to the one shown on the surface plot in (c). Applied catalyst loading: 0.02 mg cm^{-2}.

to metallic Sn — similar degradation/dissolution effects were previously reported to accompany the reduction/re-oxidation cycles of, for example, gold [75] and platinum [76] oxide surfaces.

3.4. Potential-induced catalyst degradation: Implications on the product distribution of CO_2 electrolysis

The indications of *operando* Raman spectroscopy about the potential induced oxidation state changes of SnO_2NPs@rGO are also in agreement with the measured *FE*s of formate production. In order to show this, we carried out electrolyses in a *p*H = 8.5 bicarbonate solution at different electrode potentials and used combined ion chromatography (in the solution) and on-line gas chromatographic headspace analysis to determine the product range of the reaction. By the means of chromatographic analyses, $HCOO^-$, CO and H_2 were the only detectable products, accounting — within range of experimental error — for an altogether 100% Faradaic efficiency.

The product distribution of electrolyses, lasting for 1 hour at a given potential, were calculated by determining the amount of substance generated from each product, and then comparing these amounts to the total charge consumption. Charges, for 1 hour electrolyses, are shown in Figure 7(a) as a function of the applied potential; the product distribution is shown in Figure 7(b). This figure clearly shows that at potentials not exceeding −1.1 V *vs.* Ag|AgCl in the cathodic direction, formate is the primary product of electrolysis (with some smaller amount of CO and H_2 formed). At more negative potentials, however, the selectivity towards the formation of formate drops, and HER becomes the dominant reaction.

If we compare *operando* acquired Raman spectra, shown in Figure 5(a), with the measured product distribution, shown in Figure 7(b), it becomes apparent that the highest *FE* for the production of formate can be measured when the SnO_2 NPs are — at least, partially — reduced to SnO: that is, when the catalyst is in a "mixed" oxidation state of SnO_x ($1 < x < 2$).

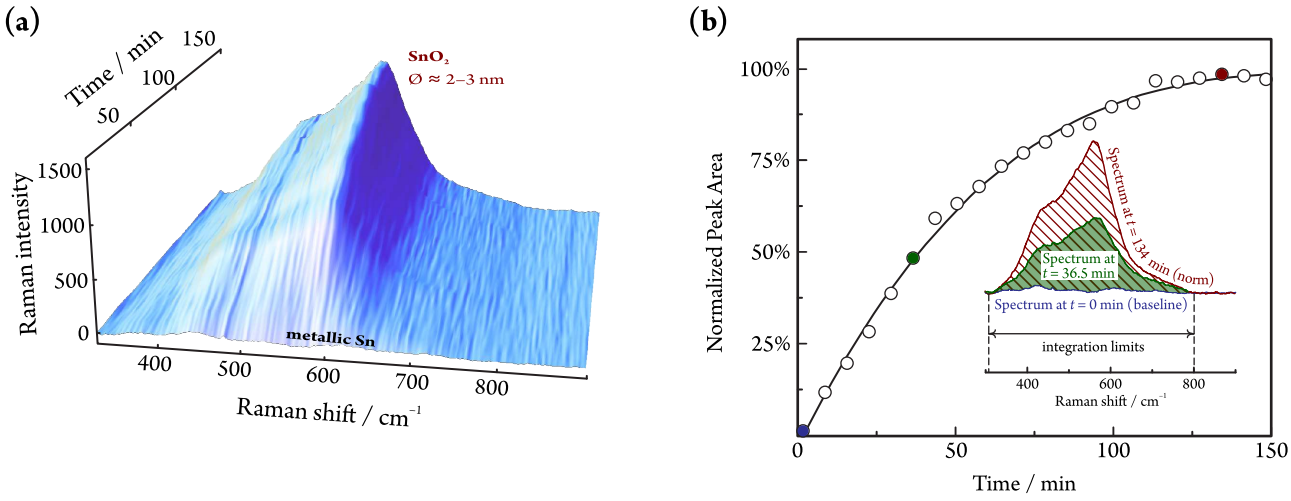

Figure 6: **(a)** Temporal evolution of Raman spectra after the electrode potential is set from –1.55 V *vs.* Ag|AgCl (where the NPs are fully reduced) to –0.25 V demonstrating the partial recovery of the SnO_2 catalyst. **(b)** Time-evolution of the relative peak intensity at a Raman shift of 580 cm^{-1}, with some selected peaks shown in the inset. Applied catalyst loading: 0.02 mg cm^{-2}.

It is interesting to note with respect to Figs. 5 and 7(b) that the practical (kinetic) stability region of SnO_2 seems to exceed the thermodynamic stability range, as it can be seen in the Pourbaix diagram [71] of Figure 7(c). Both Raman spectroscopy and the measured *FE* values indicate the presence of SnO_2 over a broad potential region where metallic Sn should already be the thermodynamically stable phase.

As it was confirmed by *operando* Raman measurements, the application of extremely negative potentials causes a full reduction of the NPs to metallic Sn, and following such an extreme reduction, the catalyst particles may only be recovered in an Sn^{IV} state at a much smaller size compared to the as-synthesised NPs (Figs. 5(c), 5(d) and 6). This effect also has consequences on the measured FE values. To demonstrate this, we subjected the NPs to reduction at −1.5 V *vs.* Ag|AgCl (lasting for several seconds) and then attempted to recover them in an SnO_2 form by subsequent conditioning at an inert potential of −0.25 V *vs.* Ag|AgCl. The conditioning at −0.25 V *vs.* Ag|AgCl lasted for a duration of 150 s, in a process similar to what resulted in the Raman spectra of Figure 6. If we then used the "recovered" NPs to measure Faradaic efficiencies, the results were very different from those obtained with as-synthesised NPs (compare Figs. 7(b) and 7(e)).

Interestingly, as shown in Figure 7(d), the overall catalytic activity of SnO_2 particles that were recovered after a severe cathodic reduction seems to be much higher than that of as-synthesised SnO_2NPs@rGO. However, the product yield of both $HCOO^-$ and CO is much lower than what was measured on the as-synthesised catalyst, as it is shown in Figure 7(e). As indicated by *operando* Raman spectroscopy, the reduced activity towards CO_2 electroreduction (and the simultaneously increased rate of HER) can be a result of the smaller particle size; *i.e.*, the irreversible degradation of the NPs caused by the previous extreme cathodic polarization. A similar selectivity *vs.* size/morphology dependence has already been described, for example, in the case of copper catalysts [77, 78].

3.5. Operando Raman investigation of catalyst stability

In the light of the discussion above, it seems expedient to determine — by the means of *operando* Raman measurements — a "safe" operation window where the rate of CO_2 reduction as well as the selectivity towards the production of formate are both high, however still no irreversible degradation is to be expected.

As shown in Figure 7(b), the application of −1.1 V *vs.* Ag|AgCl in potentiostatic electrolysis seems to be an optimum in terms of rate and selectivity. Thus, we carried out an experiment in which the electrode potential was switched periodically between –0.25 V and –1.1 V *vs.* Ag|AgCl, combined with a simultaneous acquisition of Raman spectra (Figure 8).

As shown in Figure 8(a), even the partial reduction of the NPs (taking place at −1.1 V) can cause a slight broadening of the SnO_2-related Raman peaks, which can be explained by minor degradation of the size of the NPs [72]. Nevertheless, in case of this mild reduction the overall intensity of the SnO_2-related peaks converges to a constant value after a slight initial decrease, and the formation and reoxidation of SnO seem to occur reversibly through the entire sequence of potential steps. This is in agreement with our observation that the product distribution of an electrolysis — provided, at least, that the catalyst was never exposed to potentials more negative than −1.1 V in the past — depends only on the electrode potential applied for that electrolysis, and not on the potentials where the electrode was conditioned before.

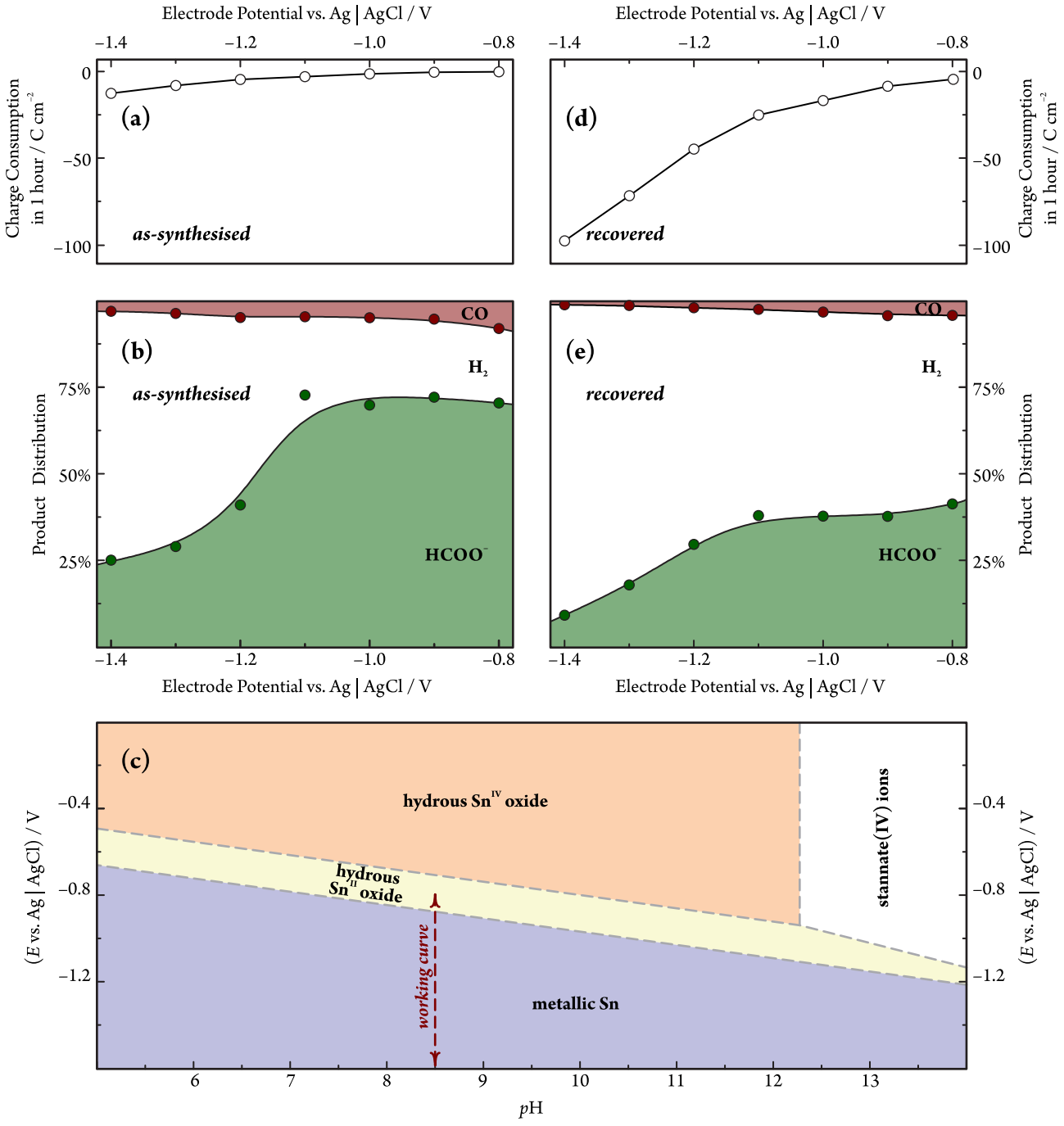

Figure 7: The implications of potential-induced catalyst degradation on the product distribution of CO_2 electrolysis in a pH = 8.5 bicarbonate solution. Applied catalyst loading: 0.5 mg cm^{-2}. Charge consumption **(a** and **d)**, as well as product distribution **(b** and **e)** data are shown for as-synthesised SnO_2NPs@rGO as well as for catalyst NPs "recovered" after an extremely negative potential excursion. The Pourbaix diagram [71] of Sn, showing thermodynamic stability regions of various Sn oxidation states, is shown as a reference **(c)**.

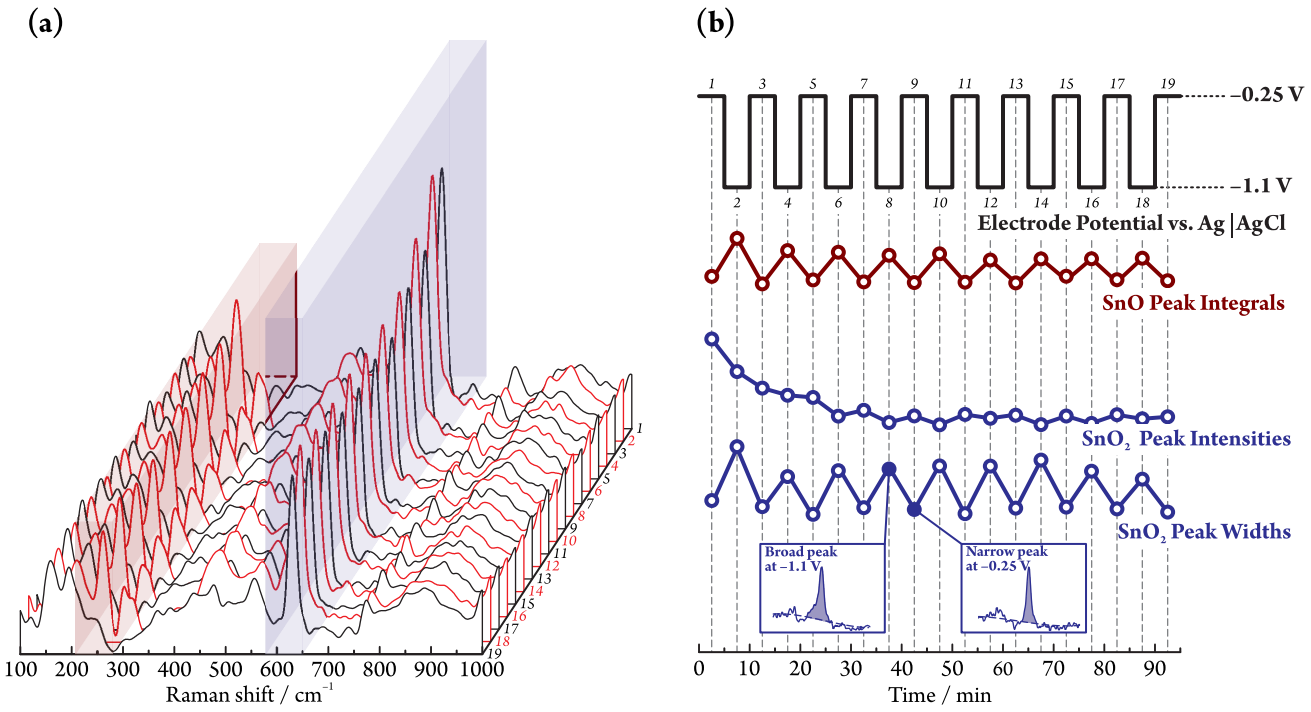

Figure 8: **(a)** Raman spectra of reduced graphene oxide supported SnO_2 NPs recorded while the electrode potential is periodically switched between –0.25 V and –1.1 V *vs.* Ag|AgCl. **(b)** The potential controlling waveform (black line) and different parameters of the peaks related to SnO and SnO_2 (red and blue lines) plotted as a function of time. The respective peaks are marked by a coloured shading in (a). Applied catalyst loading: 0.02 mg cm^{-2}.

This allows us to conclude that in order to achieve stable catalytic behaviour, the catalyst should never be exposed to strongly reducing conditions and that the potential $E \approx -1.1$ V *vs.* Ag|AgCl represents a "safe and optimal" setting.

4. Discussion

In this paper we used two *operando* methods, Raman spectroscopy and XAS, in order to investigate the potential-induced degradation (oxidation state and size changes) of SnO_2NPs@rGO. Both methods provide ample evidence for a potential-induced reduction of the catalyst particles, and they both show that under harsh cathodic conditions, the tin oxide NPs can undergo reduction to metallic tin. Although the application of such negative potentials should increase the rate of CO_2 electroreduction, in case of SnO_2NPs@rGO it leads to a severe and practically irrecoverable destruction of the catalyst and to the loss of selectivity towards the formation of formate, the desired product of CO_2 electrolysis.

We also demonstrated important practical differences between the two applied methods, *operando* XAS and Raman spectroscopy. While *operando* Raman spectroscopy clearly indicated a gradual potential-induced reduction of SnO_2NPs@rGO, involving the formation of first Sn^{II} (at mild negatvie potentials), then Sn^0 species (under harsh reductive conditions), XAS results showed no clear evidence of Sn^{II} formation. Also, according to XAS, the catalyst NPs are only partially reduced to metallic Sn (the maximal extent of reduction, according to Table 1, is only 60%), even at the extremely cathodic electrode potential of −1.7 V *vs.* Ag|AgCl. Note that the latter finding also contradicts thermodynamic expectations, according to which the presence of any tin oxides at such very negative potentials is highly unlikely [71].

The apparent contradiction outlined above can be explained if we consider the different *modi operandi* of the Raman and XAS techniques (Figure 9). Raman is a scattering spectroscopy, more sensitive to the catalyst/electrolyte solution interface. It requires the application of thin catalyst layers where no intense gas formation prevents the focusing of the laser beam. On the other hand, XAS on powder samples works better in fluorescence mode and thus for the application of XAS, thicker catalyst layers must be used. In turn, the information obtained from XAS does not only reflect the reaction-induced changes in the catalyst surface; the XAS signal contains contributions of the deeper regions.

Most importantly, the loading — *i.e.*, the mass of SnO_2NPs@rGO used to cover a given surface area of the support — that is needed for XAS measurements to be carried out at a good signal-to-noise ratio is much higher ($\sim$ 5 mg cm^{-2}) compared to that used for the Raman experiments ($\sim$ 0.02 mg cm^{-2}). It thus seems likely that

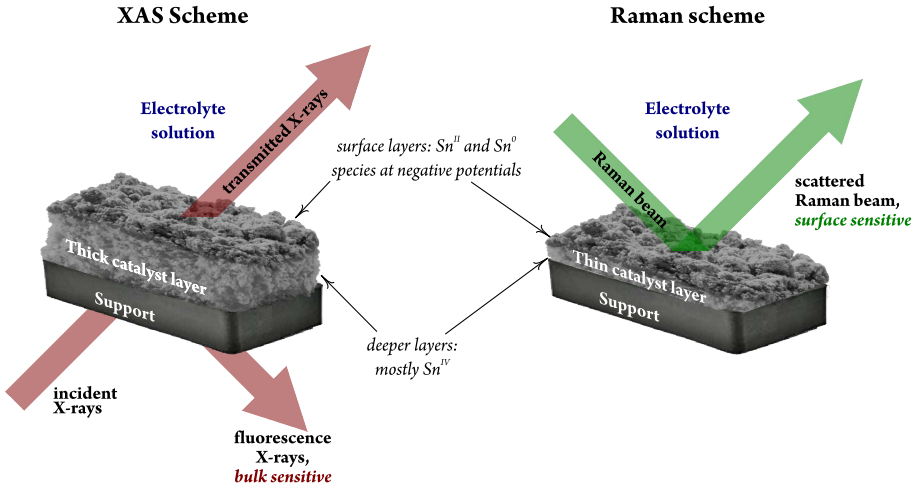

Figure 9: XAS, a fluorescence mode, and Raman, a scattering spectroscopy, applied *operando* for studying the oxidation state of SnO_2 NPs as they are used as CO_2 electroreduction catalysts. Note the difference in the geometries and the mass loading applied for the two spectroscopic methods ($\sim$ 5 mg cm^{-2} for XAS and $\sim$ 0.02 mg cm^{-2} for Raman).

under the operating conditions of XAS, some of the catalyst particles may be detached — as a result of massive H_2 evolution — from the working electrode surface and that these particles may not become fully reduced, even when large negative electrode potentials are applied.

It is also safe to assume that this detachment, and the resulting non-uniform distribution of the oxidation state of the catalyst NPs result in the non-linear growth of the catalytic rate upon the applied loading, as shown in Figure 10(a). The application of high catalyst loadings also disfavours the formation of $HCOO^-$, as it is shown in Figure 10(b). This is most likely due to transport limitations: the blockage of some active catalyst sites by H_2 formation may restrict the access of CO_2 to these sites, causing the shift of the product distribution observed in Figure 10(b).

5. Conclusion

To establish relations between the chemical structure, the activity and the selectivity of catalysts is a key step of any knowledge-driven chemical process optimization for high efficiency and maximal product yield. We believe that this approach should also be followed in innovative explorations that strive to improve catalysts for the electroreduction of CO_2.

It is a common practice in the research of electrocatalysis to correlate the catalytic activity and selectivity of a catalyst with its physico-chemical structure based on the results of *ex situ* spectroscopic characterization methods. Although this approach may sometimes be expedient — and *ex situ* characterization techniques are always inevitable parts of a thorough study —, we must point out that it is, to some extent, always based on speculation. That is, for our conclusions to hold we must always assume that a certain change in the catalyst's structure was indeed caused by the catalysed process, and not by the *ex situ* nature of the analysis method itself.

In order to leave less space for speculation, the use of *operando* spectroscopic methods for monitoring the structural changes of catalysts under real-life circumstances is always recommended; yet there can also exist important differences between different *operando* approaches that limit their applicability. The main message of this paper is to demonstrate the validity of this statement in the relation of two *operando* spectroscopies, Raman and XAS, used here for monitoring the chemical state of SnO_2NPs@rGO catalysts as they are being used for the electrolysis of CO_2.

It is an advantage of both methods that they can efficiently detect the formation of metallic Sn when the catalyst is exposed to extreme reducing conditions; this would be rather cumbersome by using *ex situ* approaches. The circumstances under which the two *operando* methods can be applied are, however, rather different.

In order to use XAS (a fluorescence mode spectroscopy), the catalyst must be applied at a high enough loading. This is a feature that makes XAS a rather robust technique: by means of XAS, loadings close to those applied in practical electrolysing cells can be studied. In turn, a large portion of the information yielded by XAS will correspond to the deeper layers of the studied catalyst and not to the actual catalyst layer / electrolyte solution interface, and thus XAS can provide only limited insight into the details of the potential-induced reduction of SnO_2NPs@rGO, occurring at the catalyst / solution boundary.

Operando Raman spectroscopy, on the other hand, is a scattering spectroscopy that can be used for the probing of catalyst particles that are in direct contact with the electrolyte solution. It can even detect the formation of an Sn^{II} state in the course of the potential-induced reduction of the SnO_2NPs@rGO catalyst, which remains unseen for

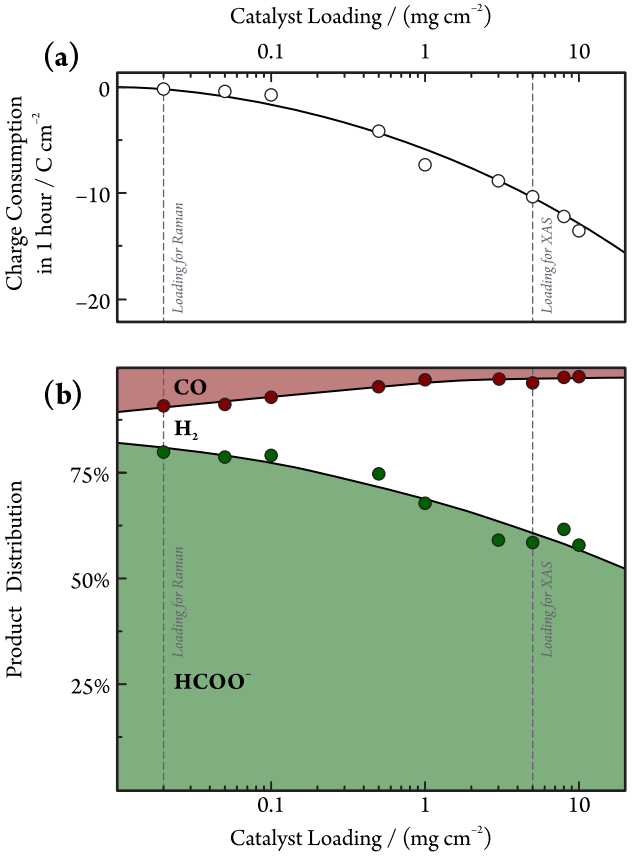

Figure 10: Charge consumption **(a)** and product distribution **(b)** measured on as-synthesised SnO_2NPs@rGO, at $E = -1.25$ V *vs.* Ag|AgCl in 1 hour electrolyses, at varied nominal catalyst loading (mass of the applied SnO_2NPs@rGO divided by the geometric surface area of the support).

XAS. In the paper we showed that this Sn^{II} state is formed exactly at those potentials that correspond to the maximum *FE* of formate production.

That *operando* Raman spectroscopy is more sensitive to the electrolyte solution/catalyst interface than XAS makes Raman spectroscopy a valuable tool for investigating the recovery of catalyst NPs. We showed that SnO_2NPs@rGO that had previously undergone complete reduction to metallic Sn can only be recovered at a smaller size in the Sn^{IV} state (compared to the size of as-synthesised NPs) and that the high $HCOO^-$ producing selectivity of these NPs is irreversibly lost. By the use of Raman spectroscopy, however, we could define an optimum electrode potential ($E \approx -1.1$ V *vs.* Ag|AgCl for SnO_2NPs@rGO in a pH = 8.5 bicarbonate solution) where a stable catalytic behaviour can still be maintained.

Acknowledgement

Support by the CTI Swiss Competence Center for Energy Research (SCCER Heat and Electricity Storage) is gratefully acknowledged.

P.B. acknowledges financial support from the Swiss National Foundation (grant No. 200020–172507).

B.R.C. acknowledges funding from the German Federal Ministry of Education and Research under grant No. 03SF0523C – "CO2EKAT" and by the European Research Council (ERC–725915, OPERANDOCAT).

S.V. acknowledges support from the National Research, Development and Innovation Office of Hungary (NKFIH grant No. PD124079, K129210).

A.K. acknowledges financial support from JSPS KAKENHI Grant-in-Aid for Scientific Research (C, grant number 17K05896).

We are grateful to Soleil (Saint-Aubin, France) for providing beam-time and to the staff of the Samba beam-line, especially to Laurent Gautier, for their experimental support.

References

[1] E. V. Kondratenko, G. Mul, J. Baltrusaitis, G. O. Larrazábal, J. Perez-Ramírez, Status and perspectives of CO_2 conversion into fuels and chemicals by catalytic, photocatalytic and electrocatalytic processes, Energy Environ. Sci. 6 (2013) 3112–3135. https://doi.org/10.1039/C3EE41272E.

[2] Y. Shao, N. M. Markovic, Prelude: The renaissance of electrocatalysis, Nano Energy 29 (2016) 1–3. https://doi.org/10.1016/j.nanoen.2016.09.025.

[3] J.-P. Jones, G. K. Surya Prakash, G. A. Olah, Electrochemical CO_2 reduction: Recent advances and current trends, Isr. J. Chem. 54 (2014) 1451–1466. https://doi.org/10.1002/ijch.201400081.

[4] M. E. Boot-Handford, J. C. Abanades, E. J. Anthony, M. J. Blunt, S. Brandani, N. Mac Dowell, J. R. Fernández, M.-Ch. Ferrari, R. Gross, J. P. Hallett, R. S. Haszeldine, Ph. Heptonstall, A. Lyngfelt, Z. Makuch, E. Mangano, R. T. J. Porter, M. Pourkashanian, G. T. Rochelle, N. Shah, J. G. Yao, P. S. Fennell, Carbon capture and storage update, Energy Environ. Sci. 7 (2014) 130–189. https://doi.org/10.1039/c3ee42350f.

[5] D. Pletcher, The cathodic reduction of carbon dioxide — What can it realistically achieve? A mini review, Electrochem. Commun. 61 (2015) 97–101. https://doi.org/10.1016/j.elecom.2015.10.006.

[6] Cs. Janáky, D. Hursán, B. Endrődi, W. Chanmanee, D. Roy, D. Liu, N. R. De Tacconi, B. H. Dennis, K. Rajeshwar, Electro- and photoreduction of carbon dioxide: The twain shall meet at copper oxide/copper interfaces, ACS Energy Lett. 1 (2016) 332–338. https://doi.org/10.1021/acsenergylett.6b00078.

[7] E. Royer, Réduction de l'acide carbonique en acide formique, Compt. Rend. Hebd. Séances Acad. Sci. 70 (1870) 731–732.

[8] J. Durst, A. Rudnev, A. Dutta, Y.-Ch. Fu, J. Herranz, V. Kaliginedi, A. Kuzume, A. Permyakova, Y. Paratcha, P. Broekmann, Th. Schmidt, Electrochemical CO_2 reduction — A critical view on fundamentals, materials and applications, Chimia 69 (2015) 769–776. https://doi.org/10.2533/chimia.2015.769.

[9] Q. Lu, F. Jiao, Electrochemical CO_2 reduction: Electrocatalyst, reaction mechanism, and process engineering, Nano Energy 29 (2016) 439–456. https://doi.org/10.1016/j.nanoen.2016.04.009.

[10] J. Herranz, J. Durst, E. Fabbri, A. Patru, X. Cheng, A. A. Permyakova, Th. J. Schmidt, Interfacial effects on the catalysis of the hydrogen evolution, oxygen evolution and CO_2-reduction reactions for (co-)electrolyzer development, Nano Energy 29 (2016) 4–28. https://doi.org/10.1016/j.nanoen.2016.01.027.

[11] H. Mistry, A. S. Varela, S. Kühl, P. Strasser, B. Roldan Cuenya, Nanostructured electrocatalysts with tunable activity and selectivity, Nat. Rev. Mater. 1 (2016) 16009. https://doi.org/10.1038/natrevmats.2016.9.

[12] D. Kopljar, N. Wagner, E. Klemm, Transferring electrochemical CO_2 reduction from semi-batch into continuous operation mode using gas diffusion electrodes, Chem. Eng. Technol. 39 (2016) 2042–2050. https://doi.org/10.1002/ceat.201600198.

[13] J.-Ph. Grote, A. R. Zeradjanin, S. Cherevko, A. Savan, B. Breitbach, A. Lugwig, K. J. J. Mayrhofer, Screening of material libraries for electrochemical CO_2 reduction catalysts – Improving selectivity of Cu by mixing with Co, J. Catal. 343 (2016) 248–256. https://doi.org/10.1016/j.jcat.2016.02.026.

[14] J. T. Feaster, Ch. Shi, E. R. Cave, T. Hatsukade, D. N. Abram, K. P. Kuhl, Ch. Hahn, J. K. Nørskov, Th. F. Jaramillo, Understanding selectivity for the electrochemical reduction of carbon dioxide to formic acid and carbon monoxide on metal electrodes, ACS Catal. 7 (2017) 4822–4827. https://doi.org/10.1021/acscatal.7b00687.

[15] G. O. Larrazábal, A. J. Martín, J. Pérez-Ramírez, Building blocks for high performance in electrocatalytic CO_2 reduction: Materials, optimization strategies, and device engineering, J. Phys. Chem. Lett. 8 (2017) 3933–3944. https://doi.org/10.1021/acs.jpclett.7b01380.

[16] F. Li, D. R. MacFarlane, J. Zhang, Recent advances in the nanoengineering of electrocatalysts for CO_2 reduction, Nanoscale 10 (2018) 6235–6260. https://doi.org/10.1039/c7nr09620h.

[17] L. R. L. Ting, B. S. Yeo, Recent advances in understanding mechanisms for the electrochemical reduction of carbon dioxide, Curr. Opin. Electrochem. 8 (2018) 126–134. https://doi.org/10.1016/j.coelec.2018.04.011.

[18] J.-H. Zhou, Y.-W. Zhang, Metal-based heterogeneous electrocatalysts for reduction of carbon dioxide and nitrogen: Mechanisms, recent advances and perspective, React. Chem. Eng., in presshttps://doi.org/10.1039/c8re00111a.

[19] J. E. Pander, D. Ren, Y. Huang, N. X. L. Wei, S. Hui, L. Hong, B. S. Yeo, Understanding the heterogeneous electrocatalytic reduction of carbon dioxide on oxide-derived catalysts, ChemElectroChem 5 (2018) 219–223. https://doi.org/10.1002/celc.201701100.

[20] Y. Hori, Electrochemical CO_2 reduction on metal electrodes, in: C. G. Vayenas, R. E. White, M. E. Gamboa-Aldeco (Eds.), Modern Aspects of Electrochemistry, Vol. 42, Springer, Berlin, 2008, pp. 89–189.

[21] A. Del Castillo, M. Alvarez-Guerra, J. Solla-Gullón, A. Sáez, V. Montiel, A. Irabien, Electrocatalytic reduction of CO_2 to formate using particulate Sn electrodes: Effect of metal loading and particle size, Appl. Energy 157 (2015) 165–173. https://doi.org/10.1016/j.apenergy.2015.08.012.

[22] H. Li, C. Oloman, The electro-reduction of carbon dioxide in a continuous reactor, J. Appl. Electrochem. 35 (2005) 955–965. https://doi.org/10.1007/s10800-005-7173-4.

[23] Anawati, G. S. Frankel, A. Agarwal, N. Sridhar, Degradation and deactivation of Sn catalyst used for CO_2 reduction as function of overpotential, Electrochim. Acta 133 (2014) 188–196. https://doi.org/10.1016/j.electacta.2014.04.057.

[24] P. Bumroongsakulsawat, G. H. Kelsall, Effect of solution pH on CO : formate formation rates during electrochemical reduction of aqueous CO_2 at Sn cathodes, Electrochim. Acta 141 (2014) 216–225. https://doi.org/10.1016/j.electacta.2014.07.057.

[25] W. Lv, R. Zhang, P. Gao, L. Lei, Studies on the faradaic efficiency for electrochemical reduction of carbon dioxide to formate on tin electrode, J. Power Sources 253 (2014) 276–281. https://doi.org/10.1016/j.jpowsour.2013.12.063.

[26] Y. Zhang, L. Chen, F. Li, Ch. D. Easton, J. Li, A. M. Bond, J. Zhang, Direct detection of electron transfer reactions underpinning the tin-catalyzed electrochemical reduction of CO_2 using Fourier-transformed AC voltammetry, ACS Catal. 7 (2017) 4846–4853. https://doi.org/10.1021/acscatal.7b01305.

[27] F. Lei, W. Liu, Y. Sun, J. Xu, K. Liu, L. Liang, T. Yao, B. Pan, Sh. Wei, Y. Xie, Metallic tin quantum sheets confined in graphene toward high-efficiency carbon dioxide electroreduction, Nat. Commun. 7 (2016) 12697. https://doi.org/10.1038/ncomms12697.

[28] F. Li, L. Chen, G. P. Knowles, D. R. MacFarlane, J. Zhang, Hierarchical mesoporous SnO_2 nanosheets on carbon cloth: A robust and flexible electrocatalyst for CO_2 reduction with high efficiency and selectivity, Angew. Chem. 129 (2016) 520–524. https://doi.org/10.1002/ange.201608279.

[29] F. Li, L. Chen, M. Xue, T. Williams, Y. Zhang, D. R. MacFarlane, J. Zhang, Towards a better Sn: Efficient electrocatalytic reduction of CO_2 to formate by Sn/SnS_2 derived from SnS_2 nanosheets, Nano Energy 31 (2017) 270–277. https://doi.org/10.1016/j.nanoen.2016.11.004.

[30] Y. Zhao, J. Liang, C. Wang, J. Ma, G. G. Wallace, Tunable and efficient tin modified nitrogen-doped carbon nanofibers for electrochemical reduction of aqueous carbon dioxide, Adv. Energy Mater. 8 (2018) 1702524. https://doi.org/10.1002/aenm.201702524.

[31] D. H. Won, Ch. H. Choi, J. Chung, M. W. Chung, E.-H. Kim, I. W. Seong, Rational design of a hierarchical tin dendrite electrode for efficient electrochemical reduction of CO_2, ChemSusChem 8 (2015) 3092–3098. https://doi.org/10.1002/cssc.201500694.

[32] J. Wu, F. G. Risalvato, F.-Sh. Ke, P. J. Pellechia, Xi.-D. Zhou, Electrochemical reduction of carbon dioxide I. Effects of the electrolyte on the selectivity and activity with Sn electrode, J. Electrochem. Soc. 159 (2012) 353–359. https://doi.org/10.1149/2.049207jes.

[33] J. Wu, F. G. Risalvato, P. P. Sharma, P. J. Pellechia, F.-Sh. Ke, Xi.-D. Zhou, Electrochemical reduction of carbon dioxide II. Design, assembly, and performance of low temperature full electrochemical cells, J. Electrochem. Soc. 160 (2013) 953–957. https://doi.org/10.1149/2.030309jes.

[34] J. Wu, F. G. Risalvato, Sh. Ma, Xi.-D. Zhou, Electrochemical reduction of carbon dioxide III. The role of oxide layer thickness on the performance of Sn electrode in a full electrochemical cell, J. Mater. Chem. 2 (2014) 1647–1651. https://doi.org/10.1039/c3ta13544f.

[35] Y. Chen, M. W. Kanan, Tin oxide dependence of the CO_2 reduction efficiency on tin electrodes and enhanced activity for tin/tin oxide thin-film catalysts, J. Am. Chem. Soc. 134 (2012) 1986–1989. https://doi.org/10.1021/ja2108799.

[36] R. Shiratsuchi, K. Hongo, G. Nogami, S. Ishimaru, Reduction of CO_2 on fluorine-doped SnO_2 thin-film electrodes, J. Electrochem. Soc. 139 (1992) 2544–2549. https://doi.org/10.1149/1.2221260.

[37] Sh. Zhang, P. Kang, Th. J. Meyer, Nanostructured tin catalysts for selective electrochemical reduction of carbon dioxide to formate, J. Am. Chem. Soc. 136 (2014) 1734–1737. https://doi.org/10.1021/ja4113885.

[38] S. Lee, J. D. Ocon, Y. Son, J. Lee, Alkaline CO_2 electrolysis towards selective and continuous $HCOO^-$ production over SnO_2 nanocatalysts, J. Phys. Chem. C 119 (2015) 4884–4890. https://doi.org/10.1021/jp512436w.

[39] M. F. Baruch, J. Pander, J. L. White, A. B. Bocarsly, Mechanistic insights into the reduction of CO_2 on tin electrodes using in situ ATR–IR spectroscopy, ACS Catal. 5 (2015) 3148–3156. https://doi.org/10.1021/acscatal.5b00402.

[40] Y. Fu, Y. Liu, Y. Li, J. Qiao, Xi.-D. Zhou, Electrochemical CO_2 reduction to formic acid on crystalline SnO_2 nanosphere catalyst, ECS Trans. 66 (2015) 53–69. https://doi.org/10.1149/06603.0053ecst.

[41] Y. Li, J. Qiao, Xi. Zhang, T. Lei, A. Girma, Y. Liu, J. Zhang, Rational design and synthesis of SnO_x electrocatalysts with coralline structure for highly improved aqueous CO_2 reduction to formate, ChemElectroChem 3 (2016) 1618–1628. https://doi.org/10.1002/celc.201600290.

[42] Ch. W. Lee, N. H. Cho, K. D. Yang, K. T. Nam, Reaction mechanisms of the electrochemical conversion of carbon dioxide to formic acid on tin oxide electrodes, ChemElectroChem 4 (2017) 1–8. https://doi.org/10.1002/celc.201700335.

[43] B. Kumar, V. Atla, J. P. Brian, S. Kumari, T. Q. Nguyen, M. Sunkara, J. M. Spurgeon, Reduced SnO_2 porous nanowires with a high density of grain boundaries as catalysts for efficient electrochemical CO_2-into-HCOOH

conversion, Angew. Chem. Int. Ed. 56 (2017) 3645–3649. https://doi.org/10.1002/anie.201612194.

[44] J. Ju, F. Héroguel, J. Luterbacher, X. Hu, Densely packed, ultra small SnO nanoparticles for enhanced activity and selectivity in electrochemical CO_2 reduction, Angew. Chem. Int. Ed. 57 (2018) 2943–2945. https://doi.org/10.1002/ange.201713003.

[45] R. Daiyan, X. Lu, Y. H. Ng, R. Amal, Surface engineered tin foil for electrocatalytic reduction of carbon dioxide to formate, Catal. Sci. Technol. 7 (2017) 2542–2550. https://doi.org/10.1039/C7CY00246G.

[46] R. Daiyan, X. Lu, W. H. Saputera, Y. H. Ng, R. Amal, Highly selective reduction of CO_2 to formate at low overpotentials achieved by a mesoporous tin oxide electrocatalyst, ACS Sustainable Chem. Eng. 6 (2018) 1670–1679. https://doi.org/10.1021/acssuschemeng.7b02913.

[47] Sh. Bashir, S. Sk. Hossain, S. ur Rahman, Sh. Ahmed, A. Al-Ahmed, M. M. Hossain, Electrocatalytic reduction of carbon dioxide on SnO_2/MWCNT in aqueous electrolyte solution, J. CO_2 Util. 16 (2016) 346–353. https://doi.org/10.1016/j.jcou.2016.09.002.

[48] J. Yu, H. Liu, Sh. Song, Y. Wang, P. Tsiakaras, Electrochemical reduction of carbon dioxide at nanostructured SnO_2/carbon aerogels: The effect of tin oxide content on the catalytic activity and formate selectivity, Appl. Catal., A 545 (2017) 159–166. https://doi.org/10.1016/j.apcata.2017.07.043.

[49] Q. Li, J. Fu, W. Zhu, Zh. Chen, B. Shen, L. Wu, Zh. Xi, T. Wang, G. Lu, J.-J. Zhu, Sh. Sun, Tuning Sn-catalysis for electrochemical reduction of CO_2 to CO via the core/shell Cu/SnO_2 structure, J. Am. Chem. Soc. 139 (2017) 4290–4293. https://doi.org/10.1021/jacs.7b00261.

[50] A. Dutta, A. Kuzume, M. Rahaman, S. Vesztergom, P. Broekmann, Monitoring the chemical state of catalysts for CO_2 electroreduction: An in operando study, ACS Catal. 5 (2015) 7498–7502. https://doi.org/10.1021/acscatal.5b02322.

[51] Y.-W.Choi, H. Mistry, B. Roldan Cuenya, New insights into working nanostructured electrocatalysts through operando spectroscopy and microscopy, Curr. Opin. Electrochem 1 (2017) 95–103. https://doi.org/10.1016/j.coelec.2017.01.004.

[52] M. A. Bañares, O. M. Guerrero-Pérez, J. L. G. Fierro, G. G. Cortez, Raman spectroscopy during catalytic operations with on-line activity measurement (operando spectroscopy): A method for understanding the active centres of cations supported on porous materials, J. Mater. Chem. 12 (2002) 3337–3342. https://doi.org/10.1039/b204494c.

[53] H. Topsøe, Developments in operando studies and in situ characterization of heterogeneous catalysts, J. Catal. 216 (2003) 155–164. https://doi.org/10.1016/s0021-9517(02)00133-1.

[54] I. E. Wachs, Ch. A. Roberts, Monitoring surface metal oxide catalytic active sites with Raman spectroscopy, Chem. Soc. Rev. 39 (2010) 5002–5017. https://doi.org/10.1039/c0cs00145g.

[55] A. Eilert, F. S. Roberts, D. Friebel, A. Nilsson, Formation of copper catalysts for CO_2 reduction with high ethylene/methane product ratio investigated with in situ X-ray absorption spectroscopy, J. Phys. Chem. Lett. 7 (2016) 1466–1470. https://doi.org/10.1021/acs.jpclett.6b00367.

[56] Q. Jia, N. Ramaswamy, U. Tylus, K. Strickland, J. Li, A. Serov, A. Artyushkova, P. Atanassov, J. Anibal, C. Gumeci, S. Calabrese Barton, M.-T. Sougrati, F. Jaouen, B. Halevi, S. Mukerjee, Spectroscopic insights into the nature of active sites in iron–nitrogen–carbon electrocatalysts for oxygen reduction in acid, Nano Energy 29 (2016) 65–82. https://doi.org/10.1016/j.nanoen.2016.03.025.

[57] D. Gao, Yi. Zhang, Zh. Zhou, F. Cai, Xi. Zhao, W. Huang, Y. Li, J. Zhu, P. Liu, F. Yang, G. Wang, Xi. Bao, Enhancing CO_2 electroreduction with the metal–oxide interface, J. Am. Chem. Soc. 139 (2017) 5652–5655. https://doi.org/10.1021/jacs.7b00102.

[58] Y. Deng, B. S. Yeo, Characterization of electrocatalytic water splitting and CO_2 reduction reactions using in situ/operando raman spectroscopy, ACS Catal. 7 (2017) 7873–7880. https://doi.org/10.1021/acscatal.7b02561.

[59] X. Li, H.-Y. Wang, H. Wang, H. Yang, W. Cai, S. Liu, B. Liu, In situ/operando characterization techniques to probe the electrochemical reactions for energy conversion, Small Methods 2 (2018) 1700395. https://doi.org/10.1002/smtd.201700395.

[60] R. Imani, Q. Zhen, R. Younesi, M. Pazoki, D. L. A. Fernandes, P. D. Mitev, T. Edvinsson, H. Tian, Unravelling in-situ formation of highly active mixed metal oxide $CuInO_2$ nanoparticles during CO_2 electroreduction, Nano Energy 49 (2018) 40–50. https://doi.org/10.1016/j.nanoen.2018.04.013.

[61] A. Kuzume, A. Dutta, S. Vesztergom, P. Broekmann, Operando Raman spectroscopy: Studies on the reactivity and stability of SnO_2 nanoparticles during electrochemical CO_2 reduction reaction, in: K. Wandelt (Ed.), Encyclopedia of Interfacial Chemistry, Surface Science and Electrochemistry, Elsevier, Amsterdam, 2018, pp. 217–226. https://doi.org/10.1016/B978-0-12-409547-2.13300-1.

[62] J. A. van Bokhoven, C. Lamberti (Eds.), X-Ray Absorption and X-Ray Emission Spectroscopy: Theory and Applications, John Wiley & Sons, Hoboken NJ, 2016.

[63] Zh. Weng, Y. Wu, W. Maoyu, J. Jiang, K. Yang, Sh. Huo, X.-F. Wang, Q. Ma, G. W. Brudvig, V. S. Batista, Y. Liang, Zh. Feng, H. Wang, Active sites of copper-complex catalytic materials for electrochemical carbon dioxide reduction, Nat. Commun. 9 (2018) 415. https://doi.org/10.1038/s41467-018-02819-7.

[64] A. Rudnev, Y.-C. Fu, I. Gjuroski, F. Stricker, J. Furrer, N. Kovács, S. Vesztergom, P. Broekmann, Transport matters: Boosting CO_2 electroreduction in mixtures of [BMIm][BF_4]/water by enhanced diffusion, ChemPhysChem 18 (2017) 3153–3162. https://doi.org/10.1002/cphc.201700737.

[65] B. Ravel, M. Newville, Athena, Artemis, Hephaestus: Data analysis for X-ray absorption spectroscopy using IFEFFIT, J. Synchrotron Rad. 12 (2005) 537–541. https://doi.org/10.1107/S0909049505012719.

[66] D. Wang, R. Kou, D. Choi, Zh. Yang, Z. Nie, J. Li, L. V. Saraf, D. Hu, J. Zhang, G. L. Graff, J. Liu, M. A. Pope, I. A. Aksay, Ternary self-assembly of ordered metal oxide – graphene nanocomposites for electrochemical energy storage, ACS Nano 4 (2010) 1587–1595. https://doi.org/10.1021/nn901819n.

[67] C. Nayral, E. Viala, P. Fau, F. Senocq, J. C. Jumas, A. Maisonnat, B. Chaudret, Synthesis of tin and tin oxide nanoparticles of low size dispersity for application in gas sensing, Chem. Eur. J. 6 (2000) 4082–4090. https://doi.org/10.1002/1521-3765(20001117)6:22<4082::aid-chem4082>3.0.co;2-s.

[68] D. Lützenkirchen-Hecht, N. Scotti, H. Jacobs, R. Frahm, XAFS investigations of tin nitrides, J. Synchrotron Rad. 8 (2001) 698–700. https://doi.org/10.1107/S0909049500015119.

[69] F. E. Oropeza, B. Mei, I. Sinev, A. E. Becerikli, M. Muhler, J. Strunk, Effect of Sn surface states on the photocatalytic activity of anatase TiO_2, App. Catal. B 140–141 (2013) 51–59. https://doi.org/10.1016/j.apcatb.2013.03.043.

[70] W. K. Choi, H. Sung, K. H. Kim, J. S. Cho, S. C. Choi, H.-J. Jung, S. K. Koh, C. M. Lee, K. Jeong, Oxidation process from SnO to SnO_2, J. Mater. Sci. Lett. 16 (1997) 1551–1554. https://doi.org/10.1023/A:1018547813759.

[71] M. Pourbaix, Atlas d'équilibres électrochimique, Gauthier-Villars et C^{ie}, Paris, 1963.

[72] A. Diéguez, A. Romano-Rodríguez, A. Vilà, J. R. Morante, The complete raman spectrum of nanometric SnO_2 particles, J. Appl. Phys. 90 (2001) 1550–1557. https://doi.org/10.1063/1.1385573.

[73] Y. Q. Guo, R. Q. Tan, X. Li, J. H. Zhao, Z. L. Luo, C. Gao, W. J. Song, Shape-controlled growth and single-crystal XRD study of submillimeter-sized single crystals of SnO, CrystEngComm 13 (2011) 5677–5680. https://doi.org/10.1039/c0ce00949k.

[74] A. Palacios-Padrós, F. Caballero-Briones, I. Díez-Pérez, F. Sanz, Tin passivation in alkaline media: Formation of SnO microcrystals as hydroxyl etching product, Electrochim. Acta 111 (2013) 837–845. https://doi.org/10.1016/j.electacta.2013.07.200.

[75] S. Vesztergom, M. Ujvári, G. G. Láng, RRDE experiments with potential scans at the ring and disk

electrodes, Electrochem. Commun. 13 (2011) 378–381. https://doi.org/10.1016/j.elecom.2011.01.032.
[76] A. Topalov, S. Cherevko, A. Zeradjanin, J. C. Meier, I. Katsounaros, K. J. J. Mayrhofer, Towards a comprehensive understanding of platinum dissolution in acidic media, Chem. Sci. 5 (2014) 631–638. https://doi.org/10.1039/c3sc52411f.
[77] A. Dutta, M. Rahaman, N. Luedi, M. Mohos, P. Broekmann, Morphology matters: Tuning the product distribution of CO_2 electroreduction on oxide-derived Cu foam catalysts, ACS Catal. 6 (2016) 3804–3814. https://doi.org/10.1021/acscatal.6b00770.
[78] R. Reske, H. Mistry, F. Behafarid, B. Roldan Cuenya, P. Strasser, Particle size effects in the catalytic electroreduction of CO_2 on Cu nanoparticles, J. Am. Chem. Soc. 136 (2014) 6978–6986. https://doi.org/10.1021/ja500328k.

Dr. Abhijit Dutta received his Ph.D. in chemistry from the Indian Institute of Engineering Science and Technology, Shibpur, in 2012. The same year he started his post-doctoral work at the National University of Singapore. Since 2014 he works as a post-doctoral researcher in Peter Broekmann's group at the University of Bern. His current research focuses on the use of Raman spectroscopy in developing novel electrocatalysts for the selective conversion of CO_2 to value-added products.

Dr. Akiyoshi Kuzume received his M.Sc. degree in chemistry from the University of Tokyo in 2001 and his Ph.D. in chemistry from the University of Liverpool in 2004. He worked as a post-doctoral fellow and as an assistant professor at the University of Alicante, at Keio University, at Tohoku University and at the University of Bern. He joined the Yamamoto ERATO Atom Hybrid Project in the Institute of Innovative Research, Tokyo Institute of Technology as a specially appointed associate professor in 2016. His research is focused on interfacial electrochemistry and electrocatalysis, by utilising combined *in situ* and *operando* spectroscopic and microscopic techniques.

Dr. Veerabhadrarao Kaliginedi obtained his M.Sc. degree in chemistry at the Indian Institute of Technology Madras, Chennai (2009) and his Ph.D. (*summa cum laude*, 2013) at the University of Bern. Currently, he is working as a post-doctoral researcher in Peter Broekmann's group in Bern. His current research interests include an electrochemical approach to molecular electronics, *in-situ* scanning probe techniques, electrocatalysis, interfacial electrochemistry and *in-situ* Raman spectroscopy.

Dr. Motiar Rahaman obtained his M.Sc. degree in chemistry at the Indian Institute of Technology Madras, Chennai (2013) and his Ph.D. (2018) at the University of Bern. The topic of his Ph.D. thesis was the electrochemical conversion of CO_2 into value-added products. Currently he is employed as a post-doctoral researcher in Peter Broekmann's research group in Bern.

Dr. Ilya Sinev obtained an M.Sc. in physics at Lomonosov Moscow State University (2004) and a Ph.D. in catalysis at the Zelinsky Institute of Organic Chemistry (Moscow). He works with Beatriz Roldán-Cuanya as a post-doctoral researcher at the Ruhr University Bochum and has several years of work experience in the area of heterogeneous (electro-) catalysis. His research is focused on studying structure-activity relationships in solid-state catalysts using surface science and synchrotron methods.

Dr. Mahdi Ahmadi obtained an M.Sc. degree in atomic and molecular physics from the University of Tehran (2011). He holds a Ph.D. (2016) from the University of Central Florida where he worked in the research group of Beatriz Roldán Cuenya. He is currently a post-doctoral research associate at Cornell University. His current research interests include electrocatalytic processes as well as the synthesis, characterization, and electrocatalytic properties of metal alloys and oxide nanoparticles with application in fuel cells.

Prof. Dr. Beatriz Roldán Cuenya received a B.Sc. in physics from the University of Oviedo (Spain, 1998) and a Ph.D. in physics from the University of Duisburg-Essen (Germany, 2001). She did a post-doc in chemical engineering at the University of California, Santa Barbara (2001–2003). She was a professor of physics at the University of Central Florida (USA, 2004–2012) and at the Ruhr University Bochum (Germany, 2013–2017). Currently, she is the director of the Department of Interface Science at the Fritz-Haber Institute of the Max Planck Society (Berlin, Germany). She studies thermal and electro-catalytic processes at the nanoscale based on *operando* microscopic and spectroscopic characterization.

Dr. Soma Vesztergom obtained his M.Sc. (2010) and Ph.D. (*summa cum laude*, 2014) degrees in chemistry at the Eötvös Loránd University of Budapest. He was a post-doctoral researcher in Peter Broekmann's group at the at the University of Bern for a year (2014) and is a regular collaborator of this group since then. He was appointed assistant professor at the Eötvös Loránd University of Budapest in 2015. Soma Vesztergom's research primarily focuses on instrumental developments in electrochemistry and on the modelling of electrocatalytic processes.

Dr. Peter Broekmann obtained his M.Sc. in chemistry (1998) and a Ph.D. (2000) from the University of Bonn. After a post-doctoral stay in 2001 at the University of Twente he became project leader at the Institute of Physical Chemistry in Bonn. Since 2008 Dr. Broekmann is lecturer for electrochemistry at the University of Bern (Switzerland). His research focuses on metal deposition processes for semiconductor and electrocatalysis applications.